Precise Parameterized Modeling of Coil Inductance in Wireless Power Transfer Systems

Yue Wu, *Student Member, IEEE*, Yongbin Jiang, *Member, IEEE*, Yaohua Li, *Student Member, IEEE*, Huan Yuan, Xiaohua Wang, *Senior Member, IEEE*, and Yi Tang, *Senior Member, IEEE*

***Abstract*—To expedite the laborious design and optimization of resonant coils in wireless power transfer systems, many traditional modeling methods are studied to calculate the coil inductances based on simplified coil structures. However, coil layouts are oversimplified in these studies, especially ignoring the corners of rectangular coils, thus leading to unavoidable low calculation accuracies. Aiming at these issues, precise parametric structure models are proposed for the circular and rectangular coils, which particularly model the corners of rectangular coils as elliptic arcs for the first time. Moreover, based on the parameterized coil structures, precise parametric inductance models are developed to achieve accurate and fast inductance calculations for coils with and without ferrite plates. Particularly, the complex mutual inductances between elliptic corners and other sections in rectangular coils are precisely analyzed and modeled. Through extensive theoretical calculations and experimental verifications, the proposed parametric inductance models not only exhibit higher calculation accuracies than traditional methods but also demonstrate much faster calculation speeds than finite element method (FEM) simulations. Specifically, the proposed models for circular and rectangular coils can enhance the mean accuracy in inductance calculation by more than 13% than traditional methods. Moreover, the proposed model implemented with MATLAB and Python programs is about 3 and 6 times faster than FEM simulations, respectively.**

***Index Terms*—Parametric inductance models, parametric structure models, wireless power transfer (WPT).**

I. Introduction

WIRELESS power transfer (WPT) technologies are increasingly prevalent in various fields, including transportation electrification [1], [2], [3], [4], consumer electronics [5], [6], [7], [8], sensor networks [9], [10], and so on [11], [12], [13], [14], [15], [16].

Manuscript received 26 January 2024; revised 11 March 2024 and 8 April 2024; accepted 11 April 2024. Date of publication 16 April 2024; date of current version 16 July 2024. This work was supported in part by the Singapore Maritime Institute under Project SMI-2019-MA-02, in part by the Research Council of Norway under Project 294871, and in part by the Shanghai Sailing Program under Grant 21YF1451300. Recommended for publication by Associate Editor J. Acero. *(Corresponding authors: Yongbin Jiang; Yi Tang.)*

Yue Wu, Huan Yuan, and Xiaohua Wang are with the School of Electrical Engineering, Xi'an Jiaotong University, Xi'an 710049, China (e-mail: dywuyue@stu.xjtu.edu.cn; huanyuan@xjtu.edu.cn; xhw@mail.xjtu.edu.cn).

Yongbin Jiang, Yaohua Li, and Yi Tang are with the School of Electrical and Electronic Engineering, Nanyang Technological University, Singapore 639798 (e-mail: yongbin.jiang@ntu.edu.sg; yaohua001@e.ntu.edu.sg; yitang@ntu.edu.sg).

Color versions of one or more figures in this article are available at https://doi.org/10.1109/TPEL.2024.3389746.

Digital Object Identifier 10.1109/TPEL.2024.3389746

Recent advancements in WPT technologies have highlighted the importance of well-designed coils that play significant roles not only in improving transfer efficiency, power density, and system interoperability but also in reducing magnetic leakage flux and manufacturing costs [17]. In the realm of WPT applications, circular and rectangular coils (RCs) are two most widely used types, making their design and optimization great hotspots in the research field of WPT technologies [18], [19], [20], [21]. In [21], an optimized electrical parameter design method was proposed based on multiple boundary constraints, in which the optimized self-inductance ranges of dual-sided coils were presented. However, the authors did not provide specific coil design methods based on the obtained optimized self-inductance ranges [21], [22].

In fact, the self- and mutual inductances of coils are of great importance in satisfying multiple design objectives of WPT systems [23], [24], [25], [26]. In [25], the self- and mutual inductances of coils were obtained with finite element method (FEM) simulations and manual adjustments. Although achieving their preset design objectives of coils, the design method was quite laborious and lengthy, thus limiting its flexibility and feasibility in practical applications. In general, current coil design and optimization methods heavily rely on FEM simulations, empirical intuitions, and manual adjustments, which are not only time-consuming but also unable to pinpoint the optimal coil design in the preobtained self-inductance ranges from theoretical and practical perspectives [25], [26]. In [27], a universal coil design structure design method was proposed to quickly adjust the coil structures to meet the inductance requirements of WPT applications. The coil design and optimization were accelerated by combining inductance modeling methods and precise FEM simulations together. Unfortunately, the authors oversimplified the RC by simplifying coil corners as right angles, which not only leads to large computation errors but also prolongs the whole coil design and optimization process.

To further expedite the design and optimization process of coils, many researchers are dedicated to analytical inductance modeling methods for calculating the self- and mutual inductances of coils based on their physical structures [28], [29], [30]. In [28], a 3-D subdomain analytical model was proposed to calculate the inductances of RC. The whole power transfer space was divided into multiple subdomains and the self- and mutual inductances were obtained by solving numerous Maxwell and

boundary equations based on electromagnetic field theory. Although the calculated coil inductances were in good agreement with FEM simulations and experimental results, the modeling process was extremely complex, and the computation was quite challenging. Moreover, in [29] and [30], the multidimensional electromagnetic field models (MEFMs) have been investigated extensively for calculating the self- and mutual inductances of resonant coils. Although MEFMs can achieve relatively good accuracies in some coil inductance calculation applications, they heavily rely on strong theoretical foundations and sophisticated mathematical equations, which poses huge challenges for engineers in practical applications.

To further improve the practicability of MEFMs and reduce the modeling difficulties, some simplified modeling methods are developed to achieve fast calculations for self- and mutual inductances of coils with more straightforward mathematical equations and simplified coil layouts. In [31] and [32], circular coils (CCs) were simplified as concentric circles for faster inductance calculations. Similarly, the RC was simplified as spiral rectangles with right angles to reduce the complexity of inductance modeling [33]. Furthermore, a user-friendly method for calculating the inductances of RC was developed, which simplifies parallel straight wires with different lengths into lines of equal length [34]. In summary, these simplified modeling methods indeed reduce the computation complexity and improve the computation speed in calculating the coil inductances in WPT systems, but their computation accuracies are not satisfactory. Especially, the computation errors will be even greater for coils with ferrite plates. In addition, it has been noticed that in recent high-power WPT applications, especially EV charging [35], relatively larger corners are added to original RC, which leads to new research problems on how to precisely describe the geometries of these corners and accurately calculate corresponding coil inductances.

In this article, precise parametric structure models are proposed to accurately characterize the geometric layouts of both CC and RC. The parameterized coil structures greatly accelerate the inductance modeling process and enhance the calculation accuracies. For the first time, the corners of the RC are modeled as elliptic arcs. Moreover, based on the parameterized coil structure, a precise parametric inductance model is developed to calculate the self- and mutual inductances of RC with and without ferrite plates. Particularly, the proposed parametric inductance model offers a practical and precise approach to calculate the complex mutual inductances between elliptic corners and other sections of RC. In general, the proposed parametric inductance model not only exhibits high calculation accuracies than traditional modeling methods but also achieves faster computation speeds than FEM simulations.

The rest of this article is organized as follows. Section II presents the parametric structure models. Section III develops the parametric inductance models for coreless CCs and RCs. By combining the image current method (ICM) with the proposed precise parametric inductance model, the inductances of coils with ferrite plates are accurately calculated in Section IV. Section V presents experimental results. Finally, Section VI concludes this article.

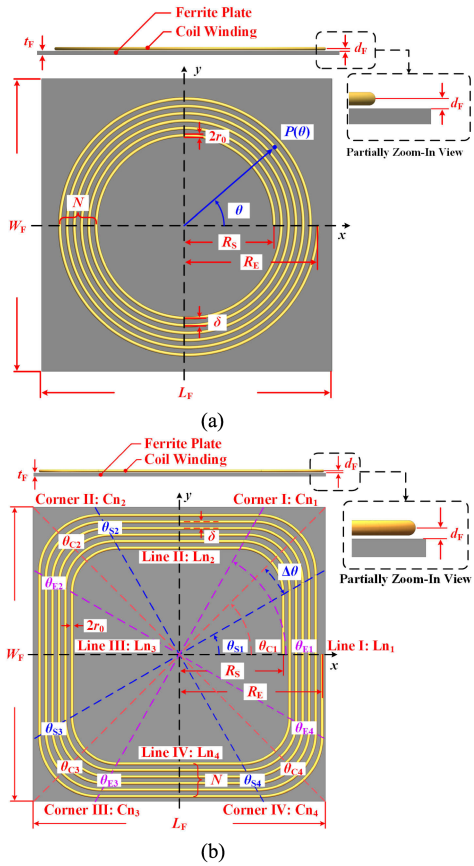

Fig. 1. Structures of different coils. (a) Structure of the CC. (b) Structure of the RC.

II. Parametric Structure Modeling of Coils

Precise descriptions of coil structures are essential to achieve precise inductance calculations. In this section, detailed parametric structure models of CCs and RCs are proposed with special focuses on the layouts of RCs and their elliptic corners.

A. Parametric Structure of CC

The CC is presented in Fig. 1(a), which consists of the coil winding and ferrite plate. The coil winding is a planar helix extending from inside to outside. By taking the coil center as the original point, a Cartesian coordinate is established, as shown in Fig. 1(a). R_S and R_E are the radii of the starting and ending points of the coil winding. δ is the winding pitch that is the center-to-center distance between two adjacent turns. r_0 is the radius of the conduction wire and N is the number of turns. W_F, L_F, and t_F are the width, length, and thickness of the ferrite plate. d_F is the distance between the center of the wire and the top surface of the ferrite plate.

For a large portion of high-power WPT systems, their operating frequencies are commonly below 100 kHz, particularly in EV wireless charging [35], where the skin and proximity effects of the coil windings can be alleviated by litz wires [36], making it reasonable to simplify the coil windings as conducting filaments. Therefore, the coordinates of the arbitrary point $P(\theta)$ of the CC, as shown in Fig. 1(a), can be calculated with the

following parametric equations:

$$\begin{cases} x(\theta) = \frac{\delta\theta}{2\pi} \cdot \cos(\theta) \\ y(\theta) = \frac{\delta\theta}{2\pi} \cdot \sin(\theta) \end{cases}, \ \theta \in [\theta_{\mathrm{S}}, \theta_{\mathrm{E}}] = \left[\frac{2\pi R_{\mathrm{S}}}{\delta}, \frac{2\pi R_{\mathrm{E}}}{\delta}\right] \quad (1)$$

where θ is the rotation angle of $P(\theta)$. The counterclockwise direction is set as the positive direction for θ and x-axis is selected as the starting axis.

B. Parametric Structure of RC

In previous studies, the geometries of RCs are generally simplified as spiral rectangles with right angles by completely ignoring four corners [33]. Corresponding inductance modeling methods based on such coil layout models are only effective and accurate when the coil corners are relatively small. However, the increasing high-power WPT applications in EV and maritime vessel charging have already begun to adopt RCs with large corners [35]. In these cases, traditional inductance modeling methods that ignore the existence of coil corners are no longer appropriate and will lead to large computation errors. In this article, a new parametric structure model is proposed to precisely describe the layout of RCs. Particularly, instead of simplifying the coil corners as right angle, accurate mathematical equations will be derived to characterize the geometries of different coil corners. It should be noted that the term "RC" mentioned in the subsequent text is actually referring to the RC with corners, as shown in Fig. 1(b).

According to Fig. 1(b), an RC consists of a coil winding and a ferrite plate. The coil winding extends from inside to outside and can be divided into eight sections, including four corners and four straight lines. The ith corner and the ith straight line of the resonant coil are abbreviated as Cn_i and Ln_i (i = 1–4), respectively. A Cartesian coordinate is built by taking the coil center as the origin point. As shown in Fig. 1(b), R_{S} is the distance between the starting point of the coil winding and y-axis, while R_{E} is the distance between the ending point of the coil winding and y-axis. δ is the winding pitch, which refers to the distance between two adjacent conduction wires. The counterclockwise direction is set as the positive direction for all angular parameters and x-axis is selected as their starting axis. $\theta_{\mathrm{C}i}$ (i = 1–4) is the center angle of Cn_i and x-axis. The starting and ending angles of Cn_i are labeled as $\theta_{\mathrm{S}i}$ and $\theta_{\mathrm{E}i}$, respectively. $\Delta\theta$ is the half of the angular difference between $\theta_{\mathrm{S}i}$ and $\theta_{\mathrm{E}i}$. Once $\theta_{\mathrm{C}i}$ and $\Delta\theta$ are determined, $\theta_{\mathrm{S}i}$ and $\theta_{\mathrm{E}i}$ can be calculated by

$$\begin{cases} \theta_{\mathrm{S}i} = \theta_{\mathrm{C}i} - \Delta\theta \\ \theta_{\mathrm{E}i} = \theta_{\mathrm{C}i} + \Delta\theta \end{cases}, (i = 1-4). \quad (2)$$

In high-frequency and high-power WPT applications, the coil winding should be continuous and smooth to not only facilitate the coil manufacturing but also avoid the magnetic field distortions between dual-sided coils and partial power loss increments in segmented winding connections. Therefore, in this article, every coil corner should be tangent to its two adjacent straight lines, which makes each corner a quarter of an ellipse. For more accurate illustrations of the coil structural characteristics, the coil corner will be denoted as the elliptic corner in the reset of this article. As shown in Fig. 2, the nth (n = 1, 2, …, N) turn of

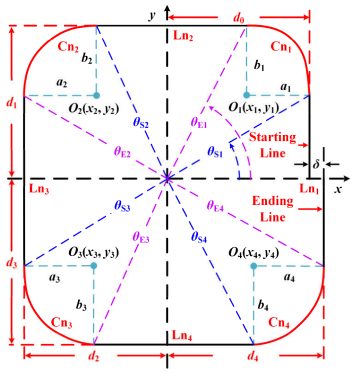

Fig. 2. Detailed structure of a single turn of the RC.

the coil winding is taken as an example. The center point of the ith elliptic corner Cn_i is labeled as $O_i(x_i, y_i)$ and the semimajor and semiminor axes of Cn_i are labeled as a_i and b_i (i = 1–4). Moreover, Ln_1 consists of starting and ending lines of the nth turn. Ln_1 and Ln_3 are parallel to y-axis, while Ln_2 and Ln_4 are parallel to x-axis. The distance between Ln_j and its parallel coordinate axis is labeled as d_j (j = 0–4). According to Figs. 1 and 2, d_j of the nth turn can be calculated by

$$d_j = R_{\mathrm{S}} + (n-1) \cdot \delta + j \cdot \delta/4, (j = 0-4). \quad (3)$$

The semimajor and semiminor axes of each elliptic corner in the nth turn can be obtained with

$$\begin{cases} a_1 = d_0 - d_1 \cdot \cot(\theta_{\mathrm{E1}}) \\ a_2 = d_2 - d_1 \cdot \tan(\theta_{\mathrm{S2}} - \pi/2) \\ a_3 = d_2 - d_3 \cdot \cot(\theta_{\mathrm{E3}} - \pi) \\ a_4 = d_4 - d_3 \cdot \tan(\theta_{\mathrm{S4}} - 3\pi/2) \end{cases},$$

$$\begin{cases} b_1 = d_1 - d_0 \cdot \tan(\theta_{\mathrm{S1}}) \\ b_2 = d_1 - d_2 \cdot \cot(\theta_{\mathrm{E2}} - \pi/2) \\ b_3 = d_3 - d_2 \cdot \tan(\theta_{\mathrm{S3}} - \pi) \\ b_4 = d_3 - d_4 \cdot \cot(\theta_{\mathrm{E4}} - 3\pi/2). \end{cases} \quad (4)$$

According to (4), the coordinates of the center points for different elliptic corners in the nth turn can be calculated by

$$\begin{cases} (x_1, y_1) = (d_0 - a_1, d_1 - b_1) \\ (x_2, y_2) = (a_2 - d_2, d_1 - b_2) \\ (x_3, y_3) = (a_3 - d_2, b_3 - d_3) \\ (x_4, y_4) = (d_4 - a_4, b_4 - d_3). \end{cases} \quad (5)$$

Therefore, the parametric equations for Cn_i in the nth turn can be derived as

$$\begin{cases} x_{\mathrm{Cn}_i}(t) = a_i \cos(t) + x_i \\ y_{\mathrm{Cn}_i}(t) = b_i \sin(t) + y_i \end{cases}, t \in \left[\frac{(i-1)\pi}{2}, \frac{i\pi}{2}\right], (i = 1-4). \quad (6)$$

Moreover, the parametric equations for different straight lines in the nth turn can be obtained with

$$\begin{cases} x_{\mathrm{Ln}_1}(t) = d_0 \\ y_{\mathrm{Ln}_1}(t) = t \end{cases}, \quad t \in [0, y_1] \cdots \text{starting line of } \mathrm{Ln}_1$$

$$\begin{cases} x_{\mathrm{Ln}_1}(t) = d_0 + \delta \\ y_{\mathrm{Ln}_1}(t) = t \end{cases}, \quad t \in [y_4, 0] \cdots \text{ending line of } \mathrm{Ln}_1 \quad (7)$$

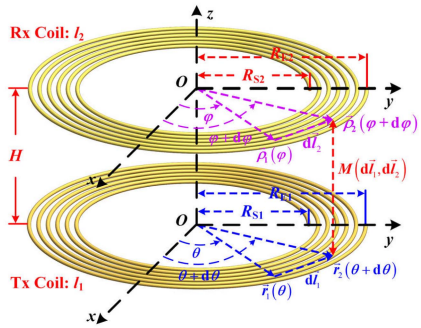

Fig. 3. Mutual coupling between two CCs.

$$\begin{cases} x_{\mathrm{Ln}_2}(t)=t \\ y_{\mathrm{Ln}_2}(t)=d_1 \end{cases}, \quad t\in[x_1,x_2]\cdots\mathrm{Ln}_2$$
$$\begin{cases} x_{\mathrm{Ln}_3}(t)=-d_2 \\ y_{\mathrm{Ln}_3}(t)=t \end{cases}, \quad t\in[y_2,y_3]\cdots\mathrm{Ln}_3 \tag{8}$$
$$\begin{cases} x_{\mathrm{Ln}_4}(t)=t \\ y_{\mathrm{Ln}_4}(t)=-d_3 \end{cases}, \quad t\in[x_3,x_4]\cdots\mathrm{Ln}_4.$$

Therefore, once all the structure parameters are obtained, the structure of the RC can be precisely modeled with (2)–(8).

III. Inductance Modeling of Coreless Coils

The self- and mutual inductances of coreless CCs and RCs will be modeled based on the obtained parametric structure models and precise coil layout descriptions. Particularly, the mutual inductances between different sections of RCs will be analyzed in-detail and modeled precisely.

A. Mutual Inductance Modeling of CC

The mutual coupling between two perfectly aligned coreless CCs is presented in Fig. 3. Although inductance modeling of CCs has been extensively studied in previous publications, a new parametric inductance modeling method is introduced in this article. The proposed method does not require complex mathematical theories or equations, which greatly reduce the modeling complexity and difficulty.

In Fig. 3, the transmitting and receiving coils are abbreviated as Tx and Rx, while their center-to-center vertical transfer distance is labeled as H. $\mathrm{d}\vec{l_1}$ and $\mathrm{d}\vec{l_2}$ are the directional curvilinear differentials of Tx and Rx, respectively. Take $\mathrm{d}\vec{l_1}$ as an example, its parametric expression can be calculated by

$$\mathrm{d}\overrightarrow{l_1}=\overrightarrow{\tau}\mathrm{ds}=\frac{[x'(\theta),y'(\theta)]}{\sqrt{[x'(\theta)]^2+[y'(\theta)]^2}}\cdot\sqrt{[x'(\theta)]^2+[y'(\theta)]^2}\mathrm{d}\theta$$
$$=[x'(\theta),y'(\theta)]\,\mathrm{d}\theta. \tag{9}$$

With (9), $\mathrm{d}\vec{l_1}$ and $\mathrm{d}\vec{l_2}$ of Tx and Rx can be obtained with (10) shown at the bottom of this page, where θ and φ are the rotation angles of Tx and Rx, respectively. Moreover, the starting and ending radii of Tx and Rx are labeled as R_{S1}, R_{E1}, R_{S2}, and R_{E2} in (10), respectively. $M(\mathrm{d}\vec{l_1},\mathrm{d}\vec{l_2})$ is the mutual inductance between $\mathrm{d}\vec{l_1}$ and $\mathrm{d}\vec{l_2}$. Therefore, the total mutual inductance between Tx and Rx can be calculated with Neumann's Formula [37], [38]

$$M=\frac{\mu_0}{4\pi}\cdot\int_{l_1}\int_{l_2}\frac{\mathrm{d}\overrightarrow{l_1}\cdot\mathrm{d}\overrightarrow{l_2}}{D\left(\mathrm{d}\overrightarrow{l_1},\mathrm{d}\overrightarrow{l_2}\right)} \tag{11}$$

where μ_0 is the vacuum permeability, and l_1 and l_2 are the directional integration paths for $\mathrm{d}\vec{l_1}$ and $\mathrm{d}\vec{l_2}$, respectively. $D(\mathrm{d}\vec{l_1},\mathrm{d}\vec{l_2})$ is the distance between $\mathrm{d}\vec{l_1}$ and $\mathrm{d}\vec{l_2}$, which can be calculated with (12) shown at the bottom of the next page, where δ_1 and δ_2 are the winding pitches of Tx and Rx, respectively. Therefore, (11) can be rewritten as (13) shown at the bottom of the next page, based on (10) and (12). When the structure parameters of target CCs are determined, their mutual inductance can then be obtained with (13).

B. Mutual Inductance Modeling of RC

The mutual coupling between two perfectly aligned coreless RCs is presented in Fig. 4. Due to the existence of multiple sections of RC windings, the magnetic coupling between different coil sections should be analyzed and calculated separately.

For elliptic corners, Cn_1 is taken as an example. As shown in Fig. 4(a), Cn_1 will magnetically couple with all sections of Rx, and their mutual inductances should be calculated individually. Ln_1 is taken as an example for the mutual inductance calculations of straight lines. As shown in Fig. 4(b), the mutual inductances between perpendicular conduction lines can be regarded as zero and only the mutual inductances between parallel conduction wires need to be calculated. Therefore, Ln_1 will only couple with Ln_1', Ln_3', and four elliptic corners in Rx. In general, the total mutual inductance between Tx and Rx can be obtained by adding up all mutual inductance components between different coil sections together.

To be more specific, the curvilinear differentials of Cn_i can be derived based on (6) and (9), which are

$$\begin{cases} \mathrm{d}x_{\mathrm{Cn}_i}(t)=-a_i\sin(t) \\ \mathrm{d}y_{\mathrm{Cn}_i}(t)=b_i\cos(t) \end{cases}, t\in\left[\frac{(i-1)\pi}{2},\frac{i\pi}{2}\right], (i=1-4). \tag{14}$$

$$\begin{cases} \mathrm{d}\overrightarrow{l_1}(\theta)=\left(\frac{\delta_1}{2\pi}\cdot\cos(\theta)-\frac{\delta_1}{2\pi}\cdot\theta\cdot\sin(\theta),\frac{\delta_1}{2\pi}\cdot\sin(\theta)+\frac{\delta_1}{2\pi}\cdot\theta\cdot\cos(\theta)\right)\cdot\mathrm{d}\theta,\theta\in\left[\frac{2\pi R_{\mathrm{S1}}}{\delta_1},\frac{2\pi R_{\mathrm{E1}}}{\delta_1}\right] \\ \mathrm{d}\overrightarrow{l_2}(\varphi)=\left(\frac{\delta_2}{2\pi}\cdot\cos(\varphi)-\frac{\delta_2}{2\pi}\cdot\varphi\cdot\sin(\varphi),\frac{\delta_2}{2\pi}\cdot\sin(\varphi)+\frac{\delta_2}{2\pi}\cdot\varphi\cdot\cos(\varphi)\right)\cdot\mathrm{d}\varphi,\varphi\in\left[\frac{2\pi R_{\mathrm{S2}}}{\delta_2},\frac{2\pi R_{\mathrm{E2}}}{\delta_2}\right] \end{cases} \tag{10}$$

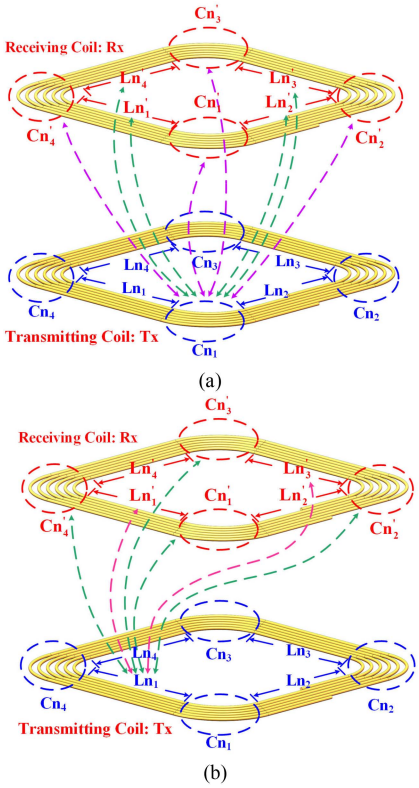

Fig. 4. Mutual coupling between two RC. (a) Coupling between Cn_1 and Rx. (b) Coupling between Ln_1 and Rx.

Similarly, the differentials of different straight lines can be derived from (7) and (8), which are

$$\begin{cases} \mathrm{d}x_{\mathrm{Ln}_1}(t) = 0 \\ \mathrm{d}y_{\mathrm{Ln}_1}(t) = 1 \end{cases}, t \in [0, y_1] \cup [y_4, 0] \cdots \mathrm{Ln}_1$$
$$\begin{cases} \mathrm{d}x_{\mathrm{Ln}_2}(t) = 1 \\ \mathrm{d}y_{\mathrm{Ln}_2}(t) = 0 \end{cases}, t \in [x_1, x_2] \cdots \mathrm{Ln}_2$$
$$\begin{cases} \mathrm{d}x_{\mathrm{Ln}_3}(t) = 0 \\ \mathrm{d}y_{\mathrm{Ln}_3}(t) = 1 \end{cases}, t \in [y_2, y_3] \cdots \mathrm{Ln}_3$$
$$\begin{cases} \mathrm{d}x_{\mathrm{Ln}_4}(t) = 1 \\ \mathrm{d}y_{\mathrm{Ln}_4}(t) = 0 \end{cases}, t \in [x_3, x_4] \cdots \mathrm{Ln}_4. \quad (15)$$

Accordingly, the mutual inductances between different coil sections of Tx and Rx can be classified into three types that are the mutual inductance between two elliptic corners Cn_i and Cn'_j (denoted as $M[\mathrm{Cn}_i, \mathrm{Cn}'_j]$), the mutual inductance between two straight lines Ln_i and Ln'_j (denoted as $M[\mathrm{Ln}_i, \mathrm{Ln}'_j]$), and the mutual inductance between an elliptic corner Cn_i and a straight line Ln'_j (denoted as $M[\mathrm{Cn}_i, \mathrm{Ln}'_j]$) ($i, j$ = 1–4). Their corresponding parametric equations are presented in (16) shown at the bottom of the next page, and more detailed mathematic equations for the mutual inductances between different coil sections can be obtained by substituting corresponding curvilinear differentials in (14) and (15) into (16). Finally, the mutual inductance between Tx and Rx, M[Tx, Rx] can be obtained with

$$M[\mathrm{Tx}, \mathrm{Rx}] = \sum_{i=1}^{4}\sum_{j=1}^{4}\left\{M\left[\mathrm{Cn}_i, \mathrm{Cn}'_j\right] + M\left[\mathrm{Cn}_i, \mathrm{Ln}'_j\right] + M\left[\mathrm{Ln}_i, \mathrm{Cn}'_j\right] + M\left[\mathrm{Ln}_i, \mathrm{Ln}'_j\right]\right\}. \quad (17)$$

C. Self-Inductance Modeling of Coils

To reduce the inductance calculation complexity, the geometric mean distance (GMD) method [38] is adopted in this article to calculate the self-inductance of coreless coil. In GMD method, the self-inductance of coreless coil is equivalently replaced by the mutual inductance between two identical coreless coils under perfect alignment when $H = g$. Here, g is the GMD of the target coil which only relates to the cross-sectional shape and size of conduction wires. For conduction wires with circular cross sections, g can be obtained by

$$g = r_0 \cdot e^{-0.25} \quad (18)$$

where r_0 is the radius of the conduction wire. Take Tx as an example, its self-inductance can be calculated by

$$L_{\mathrm{Tx}} = M[\mathrm{Tx}, \mathrm{Tx}]|_{H=g} \quad (19)$$

where M[Tx, Tx] is the mutual inductance between two perfectly aligned Tx coils with $H = g$. Since the derived integration formulas for coil inductance calculations can scarcely be solved analytically, numerical integration methods should be adopted. In this article, the composite Simpson rule [39] is used as the numerical integration method to calculate corresponding coil inductances. The formula of the composite Simpson rule is presented in the following equation:

$$F(x) = \int_a^b f(x)\mathrm{d}x \approx \frac{h}{6}\left[f(a)+f(b)+4\sum_{i=1}^{m} f\left(a+\frac{(2i-1)h}{2}\right)+2\sum_{i=1}^{m-1} f(a+(ih))\right] \quad (20)$$

where a and b are the start and end of the integration range, respectively. m is the number of integration intervals, and

$$D\left(\mathrm{d}\overrightarrow{l_1}, \mathrm{d}\overrightarrow{l_2}\right) = \frac{1}{2\pi} \cdot \sqrt{\theta^2\delta_1^2 + \varphi^2\delta_2^2 - 2\delta_1\delta_2\theta\varphi\cos(\theta-\varphi) + 4\pi^2H^2} \quad (12)$$

$$M(\mathrm{Tx}, \mathrm{Rx}) = \frac{\mu_0}{4\pi}\int_{l_1}\int_{l_2}\frac{\mathrm{d}\overrightarrow{l_1}\cdot\mathrm{d}\overrightarrow{l_2}}{D\left(\mathrm{d}\overrightarrow{l_1}, \mathrm{d}\overrightarrow{l_2}\right)} = \frac{\mu_0\delta_1\delta_2}{8\pi^2}\int_{\frac{2\pi R_{\mathrm{S1}}}{\delta_1}}^{\frac{2\pi R_{\mathrm{E1}}}{\delta_1}}\int_{\frac{2\pi R_{\mathrm{S2}}}{\delta_2}}^{\frac{2\pi R_{\mathrm{E2}}}{\delta_2}}\frac{(1+\theta\varphi)\cos(\theta-\varphi)+(\varphi-\theta)\sin(\theta-\varphi)}{\sqrt{\theta^2\delta_1^2+\varphi^2\delta_2^2-2\delta_1\delta_2\theta\varphi\cos(\theta-\varphi)+4\pi^2H^2}}\mathrm{d}\theta\mathrm{d}\varphi \quad (13)$$

$h = (b\text{-}a)/m$ is the length of each integration interval. To be short, the basic working principle of this method is to divide the whole integration range of the independent variable into multiple intervals and approximately replace the integration result of each interval with the value of the integrand at the midpoint of the corresponding interval. However, as the original composite Simpson rule is designed for univariate integration, some adjustments should be added to make it applicable to bivariate integrations in this article.

Here, (13) is selected as an example to illustrate how the composite Simpson rule is applied in this article. In (13), the mutual inductance between Tx and Rx can be viewed as a bivariate function $M(\theta, \varphi)$, whose independent variables are θ and φ, respectively. According to Fig. 3, θ and φ are the rotation angles of Tx and Rx, respectively. First, θ is selected as the independent variable while φ is kept constant, and the composite Simpson rule is only applied to the univariate integrand of θ. Then, φ is viewed as the independent variable while θ is kept constant, and the composite Simpson rule is only applied to the univariate integrand of φ. After this process, (13) can be converted into (21) shown at the bottom of this page, where m is the number of divided integration intervals. $\Delta\theta$ and $\Delta\varphi$ are the lengths of different integration intervals, which can be calculated with

$$\begin{cases} \Delta\theta = (\theta_{\mathrm{E}} - \theta_{\mathrm{S}})/m \\ \Delta\varphi = (\varphi_{\mathrm{E}} - \varphi_{\mathrm{S}})/m \end{cases} \tag{22}$$

where θ_{S} and θ_{E} are the start and end angles of the independent variable θ, while φ_{E} and φ_{S} are the start and end angles of the independent variable φ. By substituting the structure parameters of CCs into (21), the corresponding coil mutual inductance can be obtained. Similarly, the double integration in (16) can also be numerically solved with the composite Simpson rule. Moreover, the composite Simpson rule can be easily implemented with MATLAB and Python programs. Once the coil structure parameters and directional curvilinear differentials are determined, they can be directly substituted into the MATLAB and Python programs to obtain the inductances of target coils.

IV. Modeling of Coils With Ferrite Plates

Ferrite plates are essential for a large portion of WPT applications to increase the transfer efficiency and suppress the magnetic leakage flux. However, ferrite plates alter the magnetic field distributions between Tx and Rx by directing stray magnetic flux toward them, making corresponding inductance modeling extremely difficult. Therefore, the ICM is widely applied to calculate the self- and mutual inductances of coils with ferrite plates [40].

A. Basic Working Principle of ICM

The self- and mutual inductances of two closely placed coils will be influenced by dual-sided ferrite plates. As shown in Fig. 5, Tx is selected as the target coil to illustrate the working principle of ICM and how these image coils are obtained via a series of image operations, while Rx is kept unchanged.

First, in Fig. 5, the top surface of the ferrite plate of Tx and the bottom surface of the ferrite plate of Rx are designated as two reference planes RP_1 and RP_2, which are marked with the red and blue dashed lines, respectively. Second, the image operation is applied to Tx by taking RP_1 as the reference plane to obtain the first image coil IC_1. Third, the image operation will be applied to IC_1 to get IC_2 by taking RP_2 as the reference. Fourth, IC_3 can be obtained from IC_2 by taking RP_1 as the reference for the image operation again. Fifth, IC_4 is obtained from IC_3 by taking RP_2 as the reference. Finally, the image operation is applied to IC_4 by taking RP_2 as the reference. The image operation will be continued for n_{ICM} times by taking RP_1 and RP_2 as the reference plane alternatively. Through this process, the influence of dual-sided ferrite plates on the self- and mutual inductances of coils can be analyzed with ICM. Similarly, Rx can also be selected as the target coil for the image operations while Tx is kept unchanged. In this article, only Tx will be selected as the target coil.

To better determine the relative positions of Tx, Rx and different image coils, RP_1 is selected as the reference plane of the vertical coordinate system and its vertical coordinate z is set to 0. The vertical coordinate of the ith image coil IC_i ($i = 1, 2,$

$$\begin{cases} M[\mathrm{Cn}_i, \mathrm{Cn}'_j] = \frac{\mu_0}{4\pi} \cdot \int_{\mathrm{Cn}_i} \int_{\mathrm{Cn}'_j} \frac{\mathrm{d}\vec{l_1} \cdot \mathrm{d}\vec{l_2}}{D(\mathrm{d}\vec{l_1}, \mathrm{d}\vec{l_2})} = \frac{\mu_0}{4\pi} \cdot \int_{\mathrm{Cn}_i} \int_{\mathrm{Cn}'_j} \frac{\mathrm{d}x_{\mathrm{Cn}_i}(t) \cdot \mathrm{d}x_{\mathrm{Cn}'_j}(t') + \mathrm{d}y_{\mathrm{Cn}_i}(t) \cdot \mathrm{d}y_{\mathrm{Cn}'_j}(t')}{\sqrt{\left(x_{\mathrm{Cn}_i}(t) - x_{\mathrm{Cn}'_j}(t')\right)^2 + \left(y_{\mathrm{Cn}_i}(t) - y_{\mathrm{Cn}'_j}(t')\right)^2 + H^2}} \cdots (\mathrm{A}) \\ M[\mathrm{Ln}_i, \mathrm{Ln}'_j] = \frac{\mu_0}{4\pi} \cdot \int_{\mathrm{Ln}_i} \int_{\mathrm{Ln}'_j} \frac{\mathrm{d}\vec{l_1} \cdot \mathrm{d}\vec{l_2}}{D(\mathrm{d}\vec{l_1}, \mathrm{d}\vec{l_2})} = \frac{\mu_0}{4\pi} \cdot \int_{\mathrm{Ln}_i} \int_{\mathrm{Ln}'_j} \frac{\mathrm{d}x_{\mathrm{Ln}_i}(t) \cdot \mathrm{d}x_{\mathrm{Ln}'_j}(t') + \mathrm{d}y_{\mathrm{Ln}_i}(t) \cdot \mathrm{d}y_{\mathrm{Ln}'_j}(t')}{\sqrt{\left(x_{\mathrm{Ln}_i}(t) - x_{\mathrm{Ln}'_j}(t')\right)^2 + \left(y_{\mathrm{Ln}_i}(t) - y_{\mathrm{Ln}'_j}(t')\right)^2 + H^2}} \cdots (\mathrm{B}) \\ M[\mathrm{Cn}_i, \mathrm{Ln}'_j] = \frac{\mu_0}{4\pi} \cdot \int_{\mathrm{Cn}_i} \int_{\mathrm{Ln}'_j} \frac{\mathrm{d}\vec{l_1} \cdot \mathrm{d}\vec{l_2}}{D(\mathrm{d}\vec{l_1}, \mathrm{d}\vec{l_2})} = \frac{\mu_0}{4\pi} \cdot \int_{\mathrm{Cn}_i} \int_{\mathrm{Ln}'_j} \frac{\mathrm{d}x_{\mathrm{Cn}_i}(t) \cdot \mathrm{d}x_{\mathrm{Ln}'_j}(t') + \mathrm{d}y_{\mathrm{Cn}_i}(t) \cdot \mathrm{d}y_{\mathrm{Ln}'_j}(t')}{\sqrt{\left(x_{\mathrm{Cn}_i}(t) - x_{\mathrm{Ln}'_j}(t')\right)^2 + \left(y_{\mathrm{Cn}_i}(t) - y_{\mathrm{Ln}'_j}(t')\right)^2 + H^2}} \cdots (\mathrm{C}) \end{cases} \tag{16}$$

$$M(\mathrm{Tx}, \mathrm{Rx}) = M(\theta, \varphi) = \frac{\Delta\theta \cdot \Delta\varphi}{36} \left[\sum_{i=1}^{m} \sum_{j=1}^{m} M(\theta_i, \varphi_j) + 4M(\theta_i, \varphi_j + \Delta\varphi) + M(\theta_i, \varphi_{j+1}) + 4M(\theta_i + \Delta\theta, \varphi_j) \right.$$
$$\left. + 16M(\theta_i + \Delta\theta, \varphi_j + \Delta\varphi) + 4M(\theta_i + \Delta\theta, \varphi_{j+1}) + M(\theta_{i+1}, \varphi_j) + 4M(\theta_{i+1}, \varphi_j + \Delta\varphi) + M(\theta_{i+1}, \varphi_{j+1}) \right]. \tag{21}$$

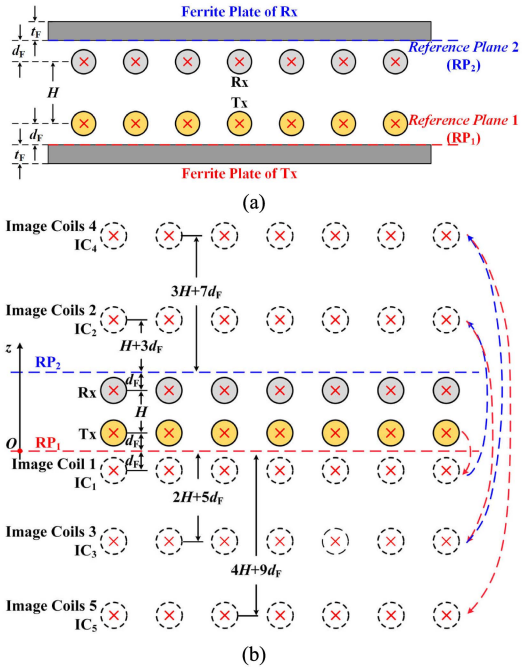

Fig. 5. Working principle of the ICM for two coils. (a) Tx and Rx with ferrite plates. (b) Image coils after image operations.

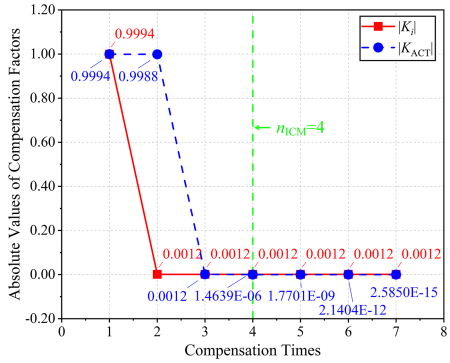

Fig. 6. Absolute values of different compensation factors.

…, n_{ICM}) can be calculated with

$$z_{\mathrm{IC}_i} = \begin{cases} 2mH + (4m+1)d_{\mathrm{F}}, i = 2m \\ -2mH - (4m+1)d_{\mathrm{F}}, i = 2m+1 \end{cases} (m = 0, 1, \ldots, N) \tag{23}$$

where N equals $n_{\mathrm{ICM}}/2$ or $(n_{\mathrm{ICM}}+1)/2$. To calculate the self- and mutual inductances between Tx and Rx, it is important to determine the vertical distances between Tx, Rx, and different IC_i. Based on the pre-obtained coordinates of IC_i in (23), the vertical distances between Tx and IC_i can be obtained with

$$h_{\mathrm{Tx\_IC}_i} = \begin{cases} 2mH + 4md_{\mathrm{F}}, i = 2m \\ 2mH + (4m+2)d_{\mathrm{F}}, i = 2m+1 \end{cases} (m = 0, 1, \ldots, N). \tag{24}$$

Similarly, the vertical distances between Rx and IC_i can be obtained with

$$h_{\mathrm{Rx\_IC}_i} = \begin{cases} (2m-1)H + 4md_{\mathrm{F}}, i = 2m \\ (2m+1)H + (4m+2)d_{\mathrm{F}}, i = 2m+1 \end{cases} (m = 0, 1, \ldots, N). \tag{25}$$

B. Self- and Mutual Inductances Modeling With ICM

Theoretically, ICM is only valid in the ideal condition, which requires the ferrite plate that has infinite thickness and width. Obviously, it is impossible in practical applications and the finite thickness and width of the ferrite plate will lead to inevitable computation errors. Therefore, the compensation factors are commonly adopted to reduce the computation errors [40], which can be calculated by

$$\begin{cases} K_1 = \frac{\mu_{\mathrm{r}}-1}{\mu_{\mathrm{r}}+1}, j = 1 \\ K_j = -K_1^{2j-3}\left(1 - K_1^2\right), j \geq 2 \end{cases} \tag{26}$$

where μ_{r} is the relative permeability of the ferrite material. j denotes that it is the jth time the corresponding reference plane that has been selected as the reference for image operation.

According to ICM, the self-inductance of Tx can be calculated with (27) shown at the bottom of this page, where L_{coil} is the coreless self-inductance of Tx and $M[\mathrm{Tx}, \mathrm{IC}_i]$ is the mutual inductance between Tx and IC_i. It is worth mentioning that L_{coil} can be calculated with (18) and (19), while $M[\mathrm{Tx}, \mathrm{IC}_i]$ can be calculated with (17) and (24).

Moreover, the mutual inductance between Tx and Rx, $M_{\mathrm{Fe}}[\mathrm{Tx}, \mathrm{Rx}]$, can be calculated with (28), where $M[\mathrm{Tx}, \mathrm{Rx}]$ is the coreless mutual inductance between Tx and Rx, which can be obtained with (17), while $M[\mathrm{Rx}, \mathrm{IC}_i]$ is the mutual inductance between Rx and IC_i, which can be calculated with (17) and (25). Notably, K_1 and K_2 are compensation factors calculated by (26).

Theoretically, the image operation should be conducted for infinite times, but in practical applications finite times of image operations will be sufficient to obtain relatively accurate results. As shown in Fig. 6, the absolute values of compensation factors are plotted. K_i is the original compensation factor in (26) while K_{ACT} is the actual compensation factor of each item in (27) and (28). Obviously, when n_{ICM} is larger than 4, $|K_{\mathrm{ACT}}|$ is small enough to be ignored, which makes it reasonable to set $n_{\mathrm{ICM}} = 4$.

$$L_{\mathrm{Tx}} = L_{\mathrm{coil}} + K_1 \cdot M[\mathrm{Tx}, \mathrm{IC}_1] + K_1^2 \cdot M[\mathrm{Tx}, \mathrm{IC}_2] + K_1^2 \cdot K_2 \cdot M[\mathrm{Tx}, \mathrm{IC}_3] + K_1^2 \cdot K_2^2 \cdot M[\mathrm{Tx}, \mathrm{IC}_4]. \tag{27}$$

$$M_{\mathrm{Fe}}[\mathrm{Tx}, \mathrm{Rx}] = M[\mathrm{Tx}, \mathrm{Rx}] + K_1 \cdot M[\mathrm{IC}_1, \mathrm{Rx}] + K_1^2 \cdot M[\mathrm{IC}_2, \mathrm{Rx}] + K_1^2 \cdot K_2 \cdot M[\mathrm{IC}_3, \mathrm{Rx}] + K_1^2 \cdot K_2^2 \cdot M[\mathrm{IC}_4, \mathrm{Rx}]. \tag{28}$$

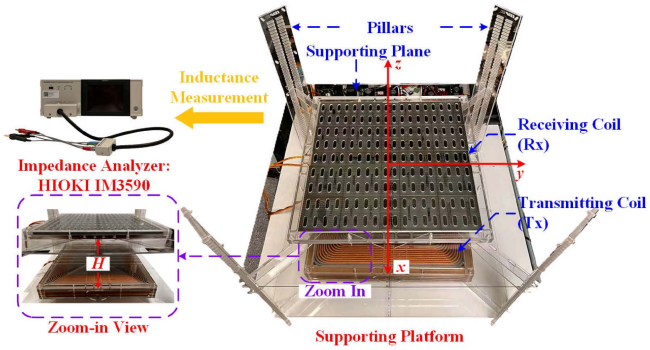

Fig. 7. Experimental platform setup.

TABLE I
DESIGN PARAMETERS OF DIFFERENT PROTOTYPE COILS

Parameter	CC	RC
R_S (mm)	122	116
R_E (mm)	194	188
N	12	12
θ_{C1} (°)	/	45
$\Delta\theta$ (°)	/	30
δ (mm)	6	6
L_F (mm)	450	450
W_F (mm)	450	450
t_F (mm)	5	5
d_F (mm)	3.1	3.1
r_0 (mm)	2.1	2.1
f(kHz)	85	85

V. EXPERIMENTAL VERIFICATION

To verify the accuracies and effectiveness of the proposed parametric inductance model, detailed experimental comparisons are conducted. Two traditional coil simplification methods are adopted as control groups. The calculated results of traditional methods and the proposed inductance models are all compared with experimental results. Meanwhile, the computing speeds of the proposed models are recorded and compared with FEM simulations.

A. Experimental Platform Setup

The experimental platform setup is presented in Fig. 7, which consists of the supporting platform and the impedance analyzer HIOKI IM3590. The whole supporting platform is made up of plastic to avoid influencing the magnetic field distributions between Tx and Rx. The transfer distance H between Tx and Rx can be adjusted by lifting or lowering the supporting plane that bears the weight of the receiving coil. The self- and mutual inductances of different coils are measured with the impedance analyzer IM3590 from HIOKI.

Based on the proposed parametric structure models of resonant coils, two prototype coils are designed, including a CC and an RC whose structure parameters are listed in Table I. In this article, the operating frequency of prototype coils is set as 85 kHz. The obtained prototype coils are presented in Fig. 8. The adopted litz wire for coil windings has the radius of 2.1 mm and 1000 strands, while TDK PC95 is selected as the ferrite material. To better validate the accuracy improvements of the proposed inductance model, two traditional coil inductance modeling methods are adopted as control groups. As shown in Fig. 9, these two modeling methods simplify the coil windings of CC and RC as concentric circles and spiral straight lines with right angles [27], [31], [32], [33].

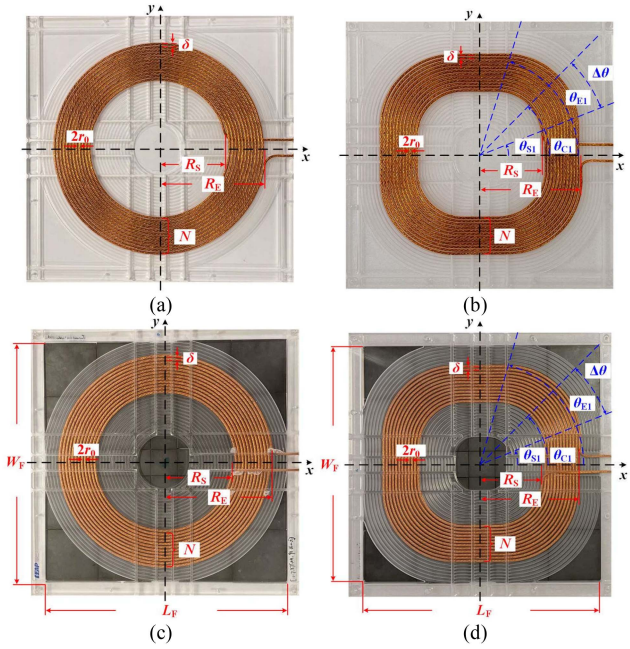

Fig. 8. Obtained prototype coils. (a) Coreless CC. (b) Coreless RC. (c) CC with the ferrite plate. (d) RC with the ferrite plate.

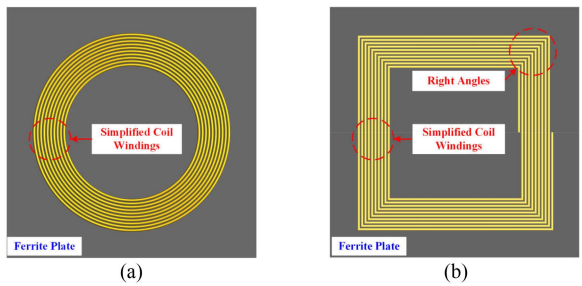

Fig. 9. Simplified coil geometries in traditional inductance modeling methods. (a) Concentric CC. (b) Spiral RC with right angles.

Moreover, delicate FEM models will be designed based on the proposed parametric structure models with the assistance of ANSYS Maxwell. Here, two 3-D FEM models of CCs and RCs are presented in Fig. 10 as examples. The structure parameters in these FEM models are the same as the structure parameters listed in Table I. The operating frequencies of corresponding FEM simulations are fixed at 85 kHz. Automatic mesh method is selected for all FEM models, whose mesh resolution is set as 7. Moreover, the length-based mesh operations are applied to the coil windings with the maximal mesh element length below 10 mm. The structure parameters of FEM models will

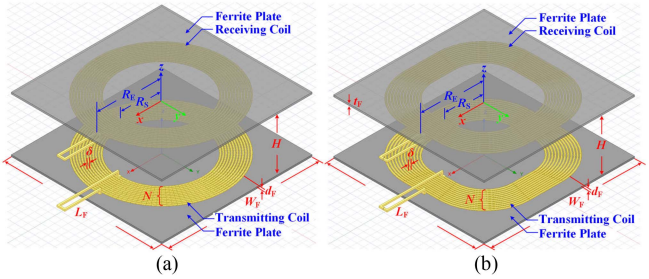

Fig. 10. Designed FEM models of (a) CC and (b) RC.

be dynamically adjusted to align with the changing prototype coil structures.

B. Accuracy Verification With Different Coils Structures

To comprehensively verify the calculation accuracies of the proposed parametric inductance models, the coil winding layouts of CC and RC will be adjusted by increasing R_{E} from 194 to 218 mm with a step length of 6 mm for CC and 188 to 212 mm with a step length of 6 mm for RC, while H is fixed at 150 mm. R_{S} of CC and RC will also increase with R_{E}, as the turns of CC and RC are kept constant. Other remaining parameters are also kept the same as listed in Table I. The FEM models, traditional methods, and the proposed parametric inductance models will all be used to calculate the self- and mutual inductances of the same prototype coil, and the simulated and calculated results will all be compared with the measured results.

The obtained results are plotted in Fig. 11, where self- and mutual inductances are plotted in solid and dashed lines, respectively. The self-inductances obtained from traditional models, the proposed models, FEM simulations, and experimental measurements are labeled as L_{T}, L_{P}, L_{SIM}, and L_{MEA}, respectively, while corresponding mutual inductances are labeled as M_{T}, M_{P}, M_{SIM}, and M_{MEA}, respectively. According to Fig. 11, the self- and mutual inductances of both CCs and RCs will increase with R_{E}. For the coreless coils, L_{P} and M_{P} are very close to L_{SIM} and M_{SIM}, which are all very close to L_{MEA} and M_{MEA}, respectively, hinting that the proposed parametric inductance models can be as accurate as the FEM simulations in coreless conditions. When the ferrite plates are added, L_{P} and M_{P} will deviate from L_{MEA} and M_{MEA}, while L_{SIM} and M_{SIM} are still very close to L_{MEA} and M_{MEA}, which means the proposed parametric inductance models will be less accurate than L_{MEA} and M_{MEA} for coils with ferrite plates. However, L_{P} and M_{P} are much closer to L_{MEA} and M_{MEA} than L_{T} and M_{T} with and without ferrite plates. Therefore, the proposed inductance models can be much more accurate than traditional modeling methods. The relative inductance calculation errors of the traditional methods, the proposed inductance models, and the FEM simulations can be calculated with

$$\varepsilon_x = \frac{x_{\mathrm{MEA}} - x}{x_{\mathrm{MEA}}} \times 100\% \tag{29}$$

where ε_x is the relative percentage error between variable x and its experimentally measured result x_{MEA}. x can be the self- or mutual inductances of different resonant coils obtained from traditional methods and proposed inductance models. In this case, x can be L_{T}, L_{P}, L_{SIM}, M_{T}, M_{P}, and M_{SIM}, respectively. x_{MEA} is the measured coil inductances, which is used as the comparison reference. To better compare the computation errors of traditional modeling methods and the proposed parametric inductance models, their corresponding calculation errors for CCs and RCs in different operating cases are listed in Tables II and III, respectively. Here, the relative calculation errors between L_{T} and L_{MEA}, L_{P} and L_{MEA}, M_{T} and M_{MEA}, as well as M_{P} and M_{MEA} are labeled as $\varepsilon_{\mathrm{TL}}$, $\varepsilon_{\mathrm{PL}}$, $\varepsilon_{\mathrm{TM}}$, and $\varepsilon_{\mathrm{PM}}$, respectively. It is obvious that the proposed parametric inductance models can achieve higher accuracies than traditional methods in calculating the inductances of CC and RC with and without ferrite plates. According to Table II, it is notably that the mean relative errors in calculating the mutual inductances of coreless CC and the self-inductances of ferrite CC can achieve peak reductions of 3.87% and 3.02%, respectively.

More significantly, as listed in Table III, the proposed parametric inductance model has much lower relative errors in calculating the self- and mutual inductances of coreless RCs. As highlighted with the bold text in Table III, the mean computation errors in self- and mutual inductance calculations for coreless RCs are reduced from 11.67% to 0.56%, and 11.27% to 1.11%, leading to significant reductions in relative errors of 11.11% and 10.16%, respectively. Moreover, the relative errors in calculating the self- and mutual inductances of coreless RCs can be reduced by as high as 11.59% and 11.14%, respectively. Although the introduction of ferrite plates will induce larger relative errors in calculating the inductances of RCs with ferrite plates, the proposed parametric inductance models can still achieve significant accuracy improvements. Compared with the traditional method, the proposed parametric inductance models can reduce the mean relative errors in self- and mutual inductance calculations of RCs with ferrite plates from 23.07% to 9.82%, and 16.09% to 4.78%, resulting in significant relative error reductions of 13.25% and 11.31%, respectively. In addition, as emphasized with the bold text in Table III, the peak relative error reductions in self- and mutual inductance calculations of RCs with ferrite plates can achieve as high as 13.65% and 13.78%, respectively.

Therefore, the proposed parametric inductance model can effectively reduce the relative errors in calculating coil inductances, particularly for RCs with elliptic corners, thus greatly improving the coil inductance modeling accuracies.

C. Comparison of Calculation Time Consumption

The proposed parametric inductance model is implemented with MATLAB and Python programs, respectively. The computation time consumption of different programs is recorded and compared with the time consumption of FEM simulations. All the programs and simulations are run on the same laptop, which is equipped with 64GB of memory, an i7-11800H CPU, and an NVIDIA 3060 GPU.

The proposed parametric inductance models are applied to the coil inductance calculations applications in Fig. 11, where R_{E} of different resonant coils are adjusted. The running time

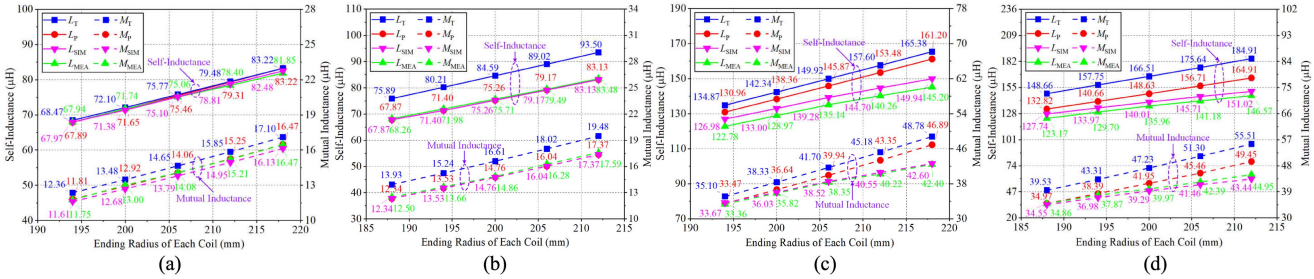

Fig. 11. Accuracy verifications for coils with different winding layouts. (a) Self- and mutual inductances of coreless CC. (b) Self- and mutual inductances of coreless RC. (c) Self- and mutual inductances of CC with ferrite plates. (d) Self- and mutual inductances of RC with ferrite plates.

TABLE II
COMPUTATIONAL ERROR COMPARISON BETWEEN TRADITIONAL METHODS AND PROPOSED MODELS FOR CC

R_E (mm)	Coreless CC				Ferrite CC			
	ε_{TL}	ε_{PL}	ε_{TM}	ε_{PM}	ε_{TL}	ε_{PL}	ε_{TM}	ε_{PM}
194	0.79%	0.06%	5.17%	0.52%	9.85%	6.67%	5.22%	0.11%
200	0.50%	0.12%	3.67%	0.66%	10.37%	7.28%	2.51%	0.82%
206	0.95%	0.53%	4.05%	0.13%	10.94%	7.94%	3.35%	1.59%
212	1.38%	1.17%	4.21%	0.24%	12.37%	9.43%	4.96%	3.13%
218	1.68%	1.67%	3.84%	0.03%	13.90%	11.02%	6.38%	4.49%
Mean ε	1.06%	0.71%	4.19%	0.32%	11.49%	8.47%	4.48%	2.03%

TABLE III
COMPUTATIONAL ERROR COMPARISON BETWEEN TRADITIONAL METHODS AND PROPOSED MODELS FOR RC

R_E (mm)	Coreless RC				Ferrite RC			
	ε_{TL}	ε_{PL}	ε_{TM}	ε_{PM}	ε_{TL}	ε_{PL}	ε_{TM}	ε_{PM}
188	11.18%	0.57%	11.48%	1.24%	20.70%	7.84%	13.40%	0.32%
194	11.43%	0.81%	11.61%	0.92%	21.63%	8.45%	14.38%	1.39%
200	11.74%	0.59%	**11.80%**	**0.66%**	22.47%	9.32%	18.16%	4.95%
206	**11.99%**	**0.40%**	10.70%	1.46%	24.41%	11.00%	**21.02%**	**7.24%**
212	12.00%	0.42%	10.74%	1.25%	**26.16%**	**12.51%**	23.49%	10.01%
Mean ε	11.67%	0.56%	11.27%	1.11%	23.07%	9.82%	16.09%	4.78%

TABLE IV
TIME CONSUMPTIONS OF DIFFERENT PROGRAMS AND FEM SIMULATIONS

Operating Case	Time consumption (mins)		
	MATLAB Programs	Python Programs	FEM simulations
Coreless CC	0.13	0.24	36.13
Ferrite CC	4.01	0.46	50.97
Coreless RC	9.43	1.18	33.13
Ferrite RC	11.48	6.22	37.33

periods with MATLAB programs, Python programs, and FEM simulations are recorded and listed in Table IV. According to Table IV, the proposed parametric inductance models exhibit faster calculation speeds than FEM simulations in different operating cases. Take the inductance calculation of RCs with ferrite plates as an example, the FEM tool takes 37.33 mins to complete the simulations while MATLAB and Python programs with the proposed parametric inductance models only take 11.48 and 6.22 mins, respectively, making them 3 times and 6 times faster than FEM simulations, respectively.

Therefore, the proposed parametric inductance model not only exhibits high accuracies in self- and mutual inductance calculations for CCs and RCs with and without ferrite plates than traditional methods but also has faster calculation speeds than FEM simulations.

VI. CONCLUSION

This article proposes novel parametric structure models to precisely describe the structures of the widely applied RCs in WPT systems, which characterize the corners of RCs as elliptic arcs for the first time. Furthermore, based on the parameterized coil structures, new parametric inductance models are developed to precisely calculate the self- and mutual inductances of the CCs and RCs with and without ferrite plates. Through extensive theoretical calculations and experimental verifications, the proposed parametric inductance models not only exhibit higher calculation accuracies than traditional methods but also demonstrate

faster calculation speeds than FEM simulations. Specifically, compared with traditional modeling methods, the proposed parametric inductance models can achieve a peak calculation accuracy enhancement of up to 13.78%. Moreover, the proposed models are implemented with MATLAB and Python programs, which are about 3 and 6 times faster than FEM simulations.

REFERENCES

[1] W. Li, H. Zhao, S. Li, J. Deng, T. Kan, and C. C. Mi, "Integrated LCC compensation topology for wireless charger in electric and plug-in electric vehicles," *IEEE Trans. Ind. Electron.*, vol. 62, no. 7, pp. 4215–4225, Jul. 2015.

[2] Y. Jiang, L. Wang, J. Fang, R. Li, R. Han, and Y. Wang, "A high-efficiency ZVS wireless power transfer system for electric vehicle charging with variable angle phase shift control," *IEEE J. Emerg. Sel. Topics Power Electron.*, vol. 9, no. 2, pp. 2356–2372, Apr. 2021.

[3] M. Wu et al., "A compact coupler with integrated multiple decoupled coils for wireless power transfer system and its anti-misalignment control," *IEEE Trans. Power Electron.*, vol. 37, no. 10, pp. 12814–12827, Oct. 2022.

[4] Y. Jiang, L. Wang, Y. Wang, J. Liu, X. Li, and G. Ning, "Analysis, design, and implementation of accurate ZVS angle control for EV battery charging in wireless high-power transfer," *IEEE Trans. Ind. Electron.*, vol. 66, no. 5, pp. 4075–4085, May 2019.

[5] Z. Zhu et al., "Efficiency optimization and power allocation of omnidirectional wireless power transfer for multiple receivers," *IEEE Trans. Ind. Electron.*, vol. 70, no. 10, pp. 9689–9699, Oct. 2023.

[6] X. Yu, J. Feng, and Q. Li, "A planar omnidirectional wireless power transfer platform for portable devices," in *Proc. IEEE Appl. Power Electron. Conf. Expo.*, 2023, pp. 1654–1661.

[7] R. Zhang et al., "Self-tuning WPT system with constant voltage output under resonance frequency shift," *IEEE Trans. Power Electron.*, vol. 39, no. 1, pp. 1713–1722, Jan. 2024.

[8] C. Liang et al., "An anti-offset CPT system with multiple pickups for mobile desktop application," *IEEE Trans. Power Electron.*, vol. 39, no. 3, pp. 3826–3841, Mar. 2024.

[9] Y. Wu, H. Yuan, R. Zhang, A. Yang, X. Wang, and M. Rong, "Low-frequency wireless power transfer via rotating permanent magnets," *IEEE Trans. Ind. Electron.*, vol. 69, no. 10, pp. 10656–10665, Oct. 2022.

[10] C. Liang, H. Yuan, R. Zhang, A. Yang, X. Wang, and M. Rong, "Analysis and design of a novel cubic WPT system in a metal environment for an enclosed sensor scenario," *IET Power Electron.*, vol. 16, pp. 1305–1319, 2023.

[11] Y. Jiang, L. Wang, J. Fang, C. Zhao, K. Wang, and Y. Wang, "A joint control with variable ZVS angles for dynamic efficiency optimization in wireless power transfer system," *IEEE Trans. Power Electron.*, vol. 35, no. 10, pp. 11064–11081, Oct. 2020.

[12] R. S. Soto, S. Maji, D. Etta, and K. K. Afridi, "A novel foreign object detection and classification algorithm for capacitive wireless charging systems," in *Proc. IEEE Wirel. Power Technol. Conf. Expo.*, 2023, pp. 1–5.

[13] S. Y. Choi, J. Huh, W. Y. Lee, and C. T. Rim, "Asymmetric coil sets for wireless stationary EV chargers with large lateral tolerance by dominant field analysis," *IEEE Trans. Power Electron.*, vol. 29, no. 12, pp. 6406–6420, Dec. 2014.

[14] K. Wang, J. Zeng, Y. Yang, and S. Y. R. Hui, "A general maximum energy efficiency tracking scheme for domino wireless power transfer systems with quasi-load-independent outputs," *IEEE Trans. Power Electron.*, vol. 39, no. 1, pp. 1840–1852, Jan. 2024.

[15] K. Wang, Y. Yang, and E. K.-W. Cheng, "Exploration of four coils magnetically coupled resonant inductive power transfer system with efficiency optimization under unsymmetrical power wiring structure," in *Proc. IEEE 49th Annu. Conf. Ind. Electron. Soc.*, 2023, pp. 1–5.

[16] Y. Li et al., "A universal parameter design method of resonant coils under multiple boundary constrains for wireless power transfer systems," in *Proc. IEEE Energy Convers. Congr. Expo.*, 2023, pp. 6489–6496.

[17] S. Jayalath and A. Khan, "Design, challenges, and trends of inductive power transfer couplers for electric vehicles: A review," *IEEE J. Emerg. Sel. Topics Power Electron.*, vol. 9, no. 5, pp. 6196–6218, Oct. 2021.

[18] S. Li, W. Li, J. Deng, T. D. Nguyen, and C. C. Mi, "A double-sided LCC compensation network and its tuning method for wireless power transfer," *IEEE Trans. Veh. Technol.*, vol. 64, no. 6, pp. 2261–2273, Jun. 2015.

[19] C. K. Lee, W. X. Zhong, and S. Y. R. Hui, "Effects of magnetic coupling of nonadjacent resonators on wireless power domino-resonator systems," *IEEE Trans. Power Electron.*, vol. 27, no. 4, pp. 1905–1916, Apr. 2012.

[20] Y. Li et al., "A new coil structure and its optimization design with constant output voltage and constant output current for electric vehicle dynamic wireless charging," *IEEE Trans. Ind. Inform.*, vol. 15, no. 9, pp. 5244–5256, Sep. 2019.

[21] Y. Jiang, L. Wang, Y. Wang, J. Liu, M. Wu, and G. Ning, "Analysis, design, and implementation of WPT system for EV'S battery charging based on optimal operation frequency range," *IEEE Trans. Power Electron.*, vol. 34, no. 7, pp. 6890–6905, Jul. 2019.

[22] Y. Jiang et al., "An optimal parameters design methodology of series-series resonant tank of wireless power transmission system for battery charging," in *Proc. IEEE Appl. Power Electron. Conf. Expo.*, 2017, pp. 1600–1605.

[23] R. Bosshard, J. W. Kolar, J. Muhlethaler, I. Stevanovic, B. Wunsch, and F. Canales, "Modeling and η-α-pareto optimization of inductive power transfer coils for electric vehicles," *IEEE J. Emerg. Sel. Topics Power Electron.*, vol. 3, no. 1, pp. 50–64, Mar. 2015.

[24] Z. Luo, X. Wei, M. G. S. Pearce, and G. A. Covic, "Multiobjective optimization of inductive power transfer double-D pads for electric vehicles," *IEEE Trans. Power Electron.*, vol. 36, no. 5, pp. 5135–5146, May 2021.

[25] K. Song et al., "Design of DD coil with high misalignment tolerance and low EMF emissions for wireless electric vehicle charging systems," *IEEE Trans. Power Electron.*, vol. 35, no. 9, pp. 9034–9045, Sep. 2020.

[26] K. Sun, J. Wang, R. Burgos, D. Boroyevich, J. Stewart, and N. Yan, "Design and multiobjective optimization of an auxiliary wireless power transfer converter in medium-voltage modular conversion systems," *IEEE Trans. Power Electron.*, vol. 37, no. 8, pp. 9944–9958, Aug. 2022.

[27] Y. Wu et al., "A universal coil structure design method with accurate numerical computation in wireless power transfer systems," in *Proc. IEEE Energy Convers. Congr. Expo.*, 2023, pp. 6497–6504.

[28] B. K. Kushwaha, G. Rituraj, and P. Kumar, "3-D analytical model for computation of mutual inductance for different misalignments with shielding in wireless power transfer system," *IEEE Trans. Transp. Electrific.*, vol. 3, no. 2, pp. 332–342, Jun. 2017.

[29] B. K. Kushwaha, G. Rituraj, and P. Kumar, "A subdomain analytical model of coil system with magnetic shields of finite dimensions and finite permeability for wireless power transfer systems," *IEEE Trans. Magn.*, vol. 56, no. 12, Dec. 2020, Art. no. 8400511.

[30] Z. Luo, S. Nie, M. Pathmanathan, W. Han, and P. W. Lehn, "3-D analytical model of bipolar coils with multiple finite magnetic shields for wireless electric vehicle charging systems," *IEEE Trans. Ind. Electron.*, vol. 69, no. 8, pp. 8231–8242, Aug. 2022.

[31] K. Fotopoulou and B. W. Flynn, "Wireless power transfer in loosely coupled links: Coil misalignment model," *IEEE Trans. Magn.*, vol. 47, no. 2, pp. 416–430, Feb. 2011.

[32] S. A. Zaini, S. H. Yusoff, M. S. A. Hanifah, E. Sulaiman, N. N. Nanda, and S. H. Badruhisham, "Design of circular pad coupler of inductive power transfer for electric vehicle (EV)," in *Proc. 8th Int. Conf. Comput. Commun. Eng.*, 2021, pp. 202–207.

[33] W. Dehui, S. Qisheng, W. Xiaohong, and Y. Fan, "Analytical model of mutual coupling between rectangular spiral coils with lateral misalignment for wireless power applications," *IET Power Electron.*, vol. 11, pp. 781–786, 2018.

[34] F. J. Lopez-Alcolea, J. V. D. Real, P. Roncero-Sanchez, and A. P. Torres, "Modeling of a magnetic coupler based on single- and double-layered rectangular planar coils with in-plane misalignment for wireless power transfer," *IEEE Trans. Power Electron.*, vol. 35, no. 5, pp. 5102–5121, May 2020.

[35] "Wireless power transfer for light-duty plug-in/electric vehicles and alignment methodology." Accessed: Oct. 10, 2022. [Online]. Available: https://www.sae.org/standards/content/j2954_202208/

[36] M. Lu and K. D. T. Ngo, "Analytical calculation of proximity-effect resistance for planar coil with litz wire and ferrite plate in inductive power transfer," *IEEE Trans. Ind. Appl.*, vol. 55, no. 3, pp. 2984–2991, May/Jun. 2019.

[37] S. R. Khan, S. K. Pavuluri, and M. P. Y. Desmulliez, "Accurate modeling of coil inductance for near-field wireless power transfer," *IEEE Trans. Microw. Theory Techn.*, vol. 66, no. 9, pp. 4158–4169, Sep. 2018.

[38] F. W. Grover, *Inductance Calculations: Working Formulas and Tables*. Chelmsford, MA, USA: Courier Corporation, 2004.

[39] T. Sauer, *Numerical Analysis*. Boston, MA, USA: Addison-Wesley Publishing, 2011.

[40] A. Zisserman, R. Saunders, and J. Caldwell, "Analytic solutions for axisymmetric magnetostatic systems involving iron," *IEEE Trans. Magn.*, vol. 23, no. 6, pp. 3895–3902, Nov. 1987.

Yue Wu (Student Member, IEEE) received the B.S. degree in electrical engineering in 2018 from the School of Electrical Engineering, Xi'an Jiaotong University, Xi'an, China, where he is currently working toward the Ph.D. degree in electrical engineering.

Since September 2022, he has been a jointly supervised Ph.D. Student with Nanyang Technological University, Singapore. His research interests include wireless power transfer, coil modeling, and coil optimization.

Yongbin Jiang (Member, IEEE) received the Ph.D. degree in electrical engineering from Xi'an Jiaotong University, Xi'an, China, in 2020.

From 2020 to 2022, he was the Director of Digital Energy Laboratory of the UNISOC (Shanghai) Technologies Company, Ltd., Shanghai, China. Since 2022, he has been a Research Fellow with Nanyang Technological University, Singapore. His research interests include wireless power transfer, high-frequency and high-power density dc/dc converters, and digital control technology.

Dr. Jiang was the recipient of the Best Paper Award of IEEE 10th International Symposium on PEDG 2019 and the Best ECCE Paper on Emerging Technology Award from IEEE PELS in 2019.

Yaohua Li (Student Member, IEEE) received the B.Eng. degree in electrical engineering from the University of Calgary, Calgary, AB, Canada, in 2020, and the M.Sc. degree in power engineering in 2021 from Nanyang Technological University, Singapore, where he is currently working toward the Ph.D. degree in electrical engineering.

His research interests include wireless power transfer, high-frequency magnetics, and AI.

Huan Yuan received the B.S. degree in electrical engineering from Southwest Jiaotong University, Shanghai, China, in 2014, and the Ph.D. degree in electrical engineering from the Department of Electrical Engineering, Xi'an Jiaotong University, Xi'an, China, in 2019.

He is currently an Associate Professor with Xi'an Jiaotong University. His research interests include intelligent perception and system in complex electromagnetic environment, wireless power transfer, and artificial intelligence.

Xiaohua Wang (Senior Member, IEEE) received the B.S. degree in electrical engineering from Chang'an University, Xi'an, China, in 2000, and the Ph.D. degree in electrical engineering from the School of Electrical Engineering, Xi'an Jiaotong University, Xi'an, in 2006.

He is currently a Professor with Xi'an Jiaotong University. He has authored or coauthored more than 120 SCI journal papers. His research interests include condition monitoring technique, fault diagnosis, and advanced sensor technique for electrical apparatus.

Yi Tang (Senior Member, IEEE) received the B.Eng. degree in electrical engineering from Wuhan University, Wuhan, China, in 2007, and the M.Sc. and Ph.D. degrees in electrical engineering from the School of Electrical and Electronic Engineering, Nanyang Technological University, Singapore, in 2008 and 2011, respectively.

From 2011 to 2013, he was a Senior Application Engineer with Infineon Technologies Asia Pacific, Singapore. From 2013 to 2015, he was a Postdoctoral Research Fellow with Aalborg University, Aalborg, Denmark. Since 2015, he has been with Nanyang Technological University, where he is currently an Associate Professor.

Dr. Tang is an Associate Editor for IEEE TRANSACTIONS ON POWER ELECTRONICS and IEEE JOURNAL OF EMERGING AND SELECTED TOPICS IN POWER ELECTRONICS .